

Method for In-Solution, High-Throughput T_1 Relaxometry Using Fluorescent Nanodiamonds

Erin S. Grant^{1,*}, Mina Barzegar Amiri Olia², Yang Li,³ Ella P. Walsh,¹ Gawain McColl,⁴
Liam T. Hall⁵, and David A. Simpson^{1,†}


¹*School of Physics, The University of Melbourne, Parkville, Victoria 3052, Australia*

²*Bio21 Molecular Science and Biotechnology Institute, Parkville, Victoria 3052, Australia*

³*School of Chemistry, The University of Melbourne, Parkville, Victoria 3052, Australia*

⁴*Florey Institute of Neuroscience and Mental Health, Parkville, Victoria 3052, Australia*

⁵*CSIRO Manufacturing, Clayton, Victoria 3168, Australia*

 (Received 2 December 2022; revised 10 May 2023; accepted 26 July 2023; published 11 September 2023)

Fluorescent nanodiamonds (FNDs) have been exploited as sensitive quantum probes for nanoscale chemical and biological sensing applications, with the majority of demonstrations to date relying on the detection of single FNDs containing either single nitrogen vacancies or nitrogen-vacancy ensembles. This places significant limits on the measurement time, throughput and statistical significance of a measured result as there is usually marked inhomogeneity within FND samples. Here, we have developed a measurement platform that can report the T_1 spin relaxation time from a large ensemble of FNDs in solution. We first describe a refined sensing protocol for this modality and then use it to identify the optimal FND size for the detection of paramagnetic targets. Our approach is simple to set up, robust and can be used for rapid material characterization for a variety of *in-situ* quantum sensing applications.

DOI: [10.1103/PhysRevApplied.20.034018](https://doi.org/10.1103/PhysRevApplied.20.034018)

I. INTRODUCTION

Fluorescent nanodiamonds (FNDs) containing the nitrogen-vacancy (N-V) defect have been developed over the last decade as a novel nanoscale sensor for a wide range of targets including pH [1], temperature [2–5], free radicals [6–9], and paramagnetic targets such as manganese, gadolinium, and iron [10–14]. The majority of characterization and chemical sensing studies that use FNDs address individual particles, as they offer high sensitivity and spatial resolution [6,13,15–18]. However, these approaches are often limited in their statistical power due to the inhomogeneous nature of FNDs' size, shape, brightness, and coherence [15]. Therefore, alternate approaches which measure the average behavior of an ensemble of FNDs offer robustness over individually sampling a small subset by reducing measurement bias. However, FND ensembles have been applied to chemical sensing exclusively in a two-dimensional (2D) setting which comes with practical limitations [14]. For example, the target may be distributed inhomogeneously across the FND ensemble, introducing large variabilities that reduce the quantitative utility of these measurements [19].

Here, we have established an all-optical, high-throughput protocol for reporting on the quantum properties of FNDs in solution. We envisage this modality as a complementary technique which offers benefits over conventional sensing approaches using N-V defects. For example, this cuvette-based approach results in a more uniform interaction between FNDs and a target, facilitating *in situ* measurement and characterization using T_1 spin relaxometry. While this study focuses on the development of this modality for measuring the T_1 spin relaxation time of dispersed FNDs, the basic apparatus can also be modified to provide quantification of the average brightness and emission spectra of samples, as previously demonstrated [15].

This work contains two main sections. First, a protocol for T_1 spin relaxometry is established, which can account for fluctuations in the fluorescence intensity of the N-V defects that are involved in a given measurement. We then apply this protocol to rapidly explore the best-sized FNDs for paramagnetic sensing of chelated Gd^{3+} ions in the form of gadobutrol, a paramagnetic chemical contrast agent often used in magnetic resonance imaging. This proof of principle demonstration shows the simplicity and high throughput of the technique, as well as the ease of performing a robust control T_1 calibration measurement.

*erin.grant@unimelb.edu.au

†simd@unimelb.edu.au

II. A PROTOCOL FOR IN-SOLUTION T_1 SPIN RELAXOMETRY

Measurements of dispersed FNDs were performed on a custom-built setup shown in Fig. 1. The apparatus consisted of a cuvette holder (Thorlabs), 532-nm (GEM, Laser Quantum) excitation laser, acousto-optical modulator (AA Electronics), and a single-photon avalanche photodiode (SPAD) (Excelitas Technologies). Laser light of 160 mW was focused to the center of the cuvette using a 150-mm plano convex lens, forming a focused beam with a waist approximately 200 μm in diameter. N- V fluorescence was extracted perpendicularly to the excitation beam through a 731 ± 137 nm bandpass filter to capture the broad fluorescence emission of the negatively charged N- V defect. The N- V fluorescence was coupled into an optical fibre (core diameter 400 μm) using an achromatic collimator with a numerical aperture of 0.54 (F950FC-A, Thorlabs) followed by detection with the SPAD. Micro cuvettes (BRAND 759200, Sigma Aldrich) were used to hold a 170 μL suspension of FNDs. The left inset of Fig. 1 shows a photo of the cuvette and holder. N- V fluorescence is visible through the filter at the front of the holder as a red line.

T_1 spin relaxation measurements were performed using the N- V defects housed within the FNDs. The N- V defect consists of a substitutional nitrogen atom and an adjacent vacancy (see right inset of Fig. 1). It is a spin-1 system, with an electronic structure shown in Fig. 2(a). The $m_s = 0$ and $m_s = \pm 1$ ground spin-state levels are separated by the zero-field splitting, $D = 2.87$ GHz. When excited from the $m_s = 0$ ground state, the N- V defect emits 30% more fluorescence than the corresponding transitions from the $m_s = \pm 1$ states, which provides a convenient method to optically report the ground spin-state populations [20,21]. This can be used to perform T_1 spin relaxometry which measures the degree of longitudinal relaxation of the N- V spin polarization, where T_1 is defined as the time at which the emission intensity reaches $1/e$ of the maximum value. The characteristic time may also be expressed as a rate, $\Gamma = 1/T_1$, which will be used here. Fluctuating magnetic field sources act to increase Γ . These magnetic field sources can come from electronic spins on or within the FND [16,22], or from external targets such as paramagnetic molecules [12] or magnetic materials [23].

To measure the T_1 spin relaxation process, a simple protocol was employed, as shown in Fig. 2(b). First, the polarizing laser pulse was used to initialize the ensemble of FNDs within the beam path into the bright, $m_s = 0$, ground state. Then, after an evolution time τ , a second laser pulse was used to read out the average spin state of the N- V ensemble, as well as repolarizing for the next measurement. Each laser pulse in the protocol was applied for the same length of time, but by varying τ , a T_1 spin relaxation curve of the form shown in Fig. 2(c) can be generated.

For an individual N- V defect, the decay profile of the measured emission intensity will be determined by its intrinsic relaxation rate, Γ_{int} , as well as that produced by the presence of target spins, Γ_{targ} , giving an emission intensity

$$I(\tau) = \mathcal{C} \exp\left(-\Gamma_{\text{int}}\tau - \sum_i^{N_T} (\Gamma_{i,\text{targ}}\tau)\right) + I(\infty), \quad (1)$$

where N_T is the number of target spins.

This becomes more complicated when considering an ensemble of FNDs as we need to sum over the total number of N- V defects:

$$I(\tau) = \sum_j^{N_{\text{N-}V}} \left[\mathcal{C} \exp\left(-\Gamma_{\text{int}}\tau - \sum_i^{N_T} (\Gamma_{i,j,\text{targ}}\tau)\right) + I(\infty) \right]_j, \quad (2)$$

where $N_{\text{N-}V}$ is the total number of N- V defects in the ensemble. In this situation, the emission intensity, $I(\tau)$, is composed of a large sum of exponentials which cannot be fitted with a single exponential function. There are two main approaches in the literature for fitting this data, both of which approximate the resulting fluorescence signal. These are a double exponential [17,18,24] and a stretched exponential [14,15,19,25]. Both approaches are experimentally derived, rather than physically motivated [26]. A stretched exponential function is preferred when there is a distribution of decay rates contributing to the measured signal, whereas a double exponential is suited to cases which involve two dominant time scales. Here, we expect a large distribution of decay rates, as we are dealing with an N- V ensemble housed by inhomogeneous FNDs [27]. This was confirmed when comparing the two fit types; fitting with a stretched exponential function proved to be more robust than a double exponential (see the Supplemental Material [28] for an example of the double exponential fits).

For the intrinsic case, where there is no target present, the stretched exponential function is given by

$$I(\tau) \approx \mathcal{C} \exp\left(-(\Gamma_{\text{int}}\tau)^p\right) + I(\infty), \quad (3)$$

where \mathcal{C} , is the spin contrast. The stretch power, p , is influenced by the variance in Γ_{int} across the FND ensemble. When a target is introduced, a second term must be added to the exponent:

$$I(\tau) \approx \mathcal{C} \exp\left(-(\Gamma_{\text{int}}\tau)^p - (\Gamma_{\text{targ}}\tau)^q\right) + I(\infty). \quad (4)$$

To isolate the effect of the target, Γ_{targ} , a control measurement is first taken to find the values of Γ_{int} and p , using Eq. (3), which are then fixed when fitting with Eq. (4). In

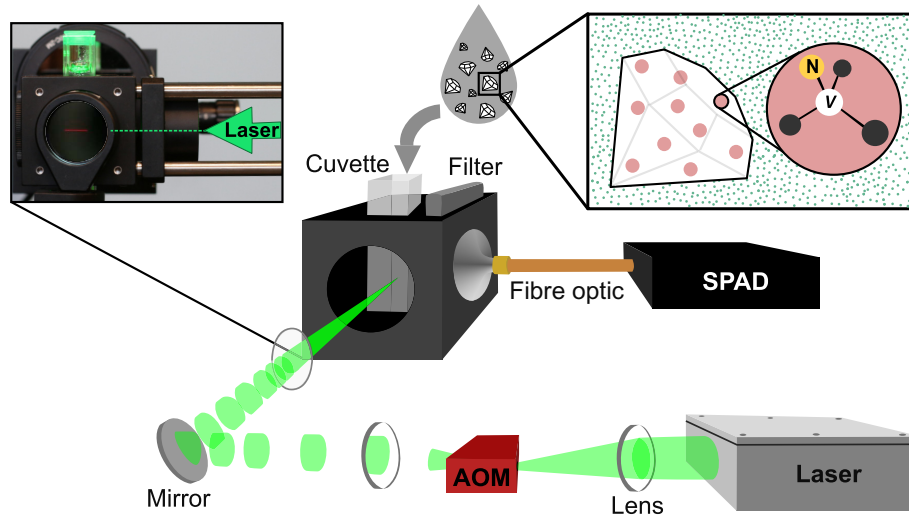


FIG. 1. Schematic of the in-solution measurement apparatus. The setup consists of a 532-nm laser which is modulated using an acousto-optical modulator. Nitrogen-vacancy (N-V) fluorescence is extracted through an optical fibre and measured on a single-photon avalanche photodiode. Top left inset: A photo of the cuvette; N-V fluorescence is visible as a thin red line through the optical filter at the front of the image. Top right inset: Quantum sensing is performed using dispersed FNDs containing the N-V defect which consists of a substitutional nitrogen atom and an adjacent vacancy.

practice, the measured stretch powers p and q are similar. This is not surprising, as they are influenced by the variance in Γ_{int} and Γ_{targ} across the FND ensemble which both depend on the geometric arrangement of the noise sources that contribute to them. In the case of Γ_{int} , this is noise that is intrinsic to the diamond, whereas for Γ_{targ} it is the target spins. In FNDs, Γ_{int} is dominated by surface spin noise [12,22,29], while the influence of the target (Γ_{targ}) will be skewed toward spins in close proximity to the surface, due to the r^{-6} dependence [12]. See the Supplemental Material [28] for a comparison of the measured values of p and q .

To control for laser fluctuations, other environmental noise, and potential N-V charge state changes across the measurement time, each data point in the T_1 curve is found by taking the ratio of the integrated emission intensity in a window at the beginning of the laser pulse (which informs on the average spin-state population of the ensemble), with the integrated intensity in a window at the end of the pulse (which represents the steady-state population of the repolarized state). The respective pulses are shown by the dotted boxes in the SPAD trace of Fig. 2(b).

The integration window widths were chosen such that they provided an optimal tradeoff between spin contrast, \mathcal{C} , and the number of photons collected per sweep. For both the signal and reference windows, this optimum was found to be a width of 10 μs . Optimization studies were also performed in order to identify the most appropriate laser pulse length as well as to establish the efficacy of taking the ratio between the signal and reference data. These investigations showed that a pulse length of 80 μs was able to polarize the N-V defects while maintaining the steady-state

intensity within 2–3% across a relaxation measurement. Taking the ratio of the signal to reference intensities was shown to account for this small variation in steady-state intensity, validating the protocol. An in-depth discussion of each of these optimization studies is presented in the Supplemental Material [28].

After establishing a T_1 measurement protocol, we studied the effect of the FND concentration on the measured T_1 relaxation curve. Our findings show that as the concentration of the FND solution is increased, the N-V spin contrast and signal to noise of the measurement both decrease, as presented in Figs. 2(e) and 2(f). These changes are attributed to scattering of the N-V fluorescence, which can impact the signal intensity and modify its temporal characteristics. This scattering effect appears to be limited to concentrations greater than 25 $\mu\text{g/ml}$. Therefore, we used FNDs with a concentration less than 25 $\mu\text{g/ml}$ for the remainder of this work. We note, however, that scattering increases with particle volume, so for smaller FND sizes it may be possible to operate at concentrations higher than 25 $\mu\text{g/mL}$ [30].

III. EXAMPLE CHARACTERIZATION AND SENSING STUDY

In-solution T_1 relaxometry has the potential to offer high-throughput measurements of large numbers of FNDs, making it useful for both characterization and quantum sensing studies. We envisage this to be a complementary method to confocal or widefield microscopy, which navigates some of the practical challenges inherent to these two

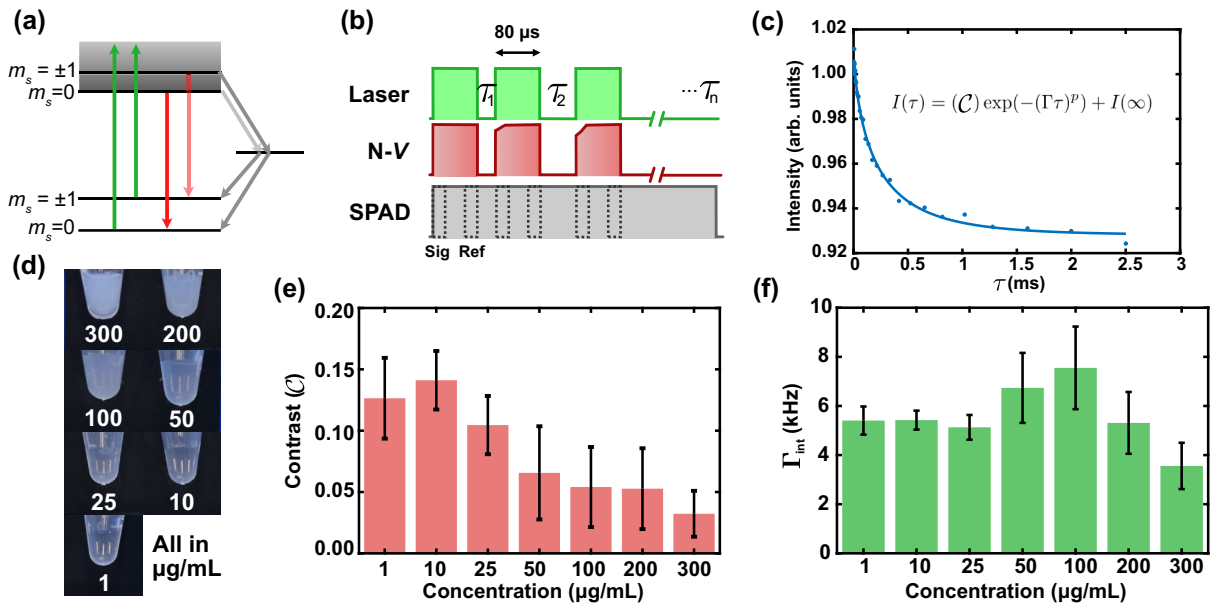


FIG. 2. In-solution T_1 relaxometry with FNDs. (a) Schematic of the energy levels of the N-V defect in diamond. These consist of triplet ground and excited states and two intermediate singlet states. (b) The T_1 sensing protocol. The N-V ensemble is polarized and read out using an 80- μs laser pulse, followed by a variable wait time τ . The N-V spin population is determined by taking the ratio of the integrated intensity in the first 10 μs of the excitation pulse to the integrated intensity in the final 10 μs of the pulse. (c) A typical T_1 spin relaxation curve measured using the pulse sequence in (b). The intensity decay is fitted with a stretched exponential equation. (d) Images of 140-nm FND suspensions in ultrapure water at concentrations ranging from 1 to 300 $\mu\text{g/mL}$. The effect of the concentration of the FNDs on the measured C (e) and Γ_{int} (f). The FND concentration has a negligible effect for values below 25 $\mu\text{g/mL}$.

conventional techniques. To assess the utility of the technique, we first identified the FND size that is most useful and then applied these FNDs to sensing Gd(III).

Evaluation of any sensor requires consideration of its dynamic range, sensitivity, and limit of detection (LOD). Ideally, a sensor will respond consistently to a wide range of concentrations with a low LOD, but it must also be able to distinguish between two samples with very similar concentrations. In the context of T_1 spin relaxometry, optimal performance within this metric will be determined by Γ_{int} , the optical noise, and the N-V depth distribution with respect to the diamond surface. If all other characteristics are equal, N-Vs with a lower Γ_{int} , offer a greater dynamic range, as the operating bandwidth will span $\Gamma_{\text{max}} - \Gamma_{\text{intrinsic}}$, where Γ_{max} is the maximum decay rate determined by the spin polarization time of the N-V defects (of the order of tens of microseconds). Meanwhile, the measurement sensitivity depends on the N-V spin contrast, photon count rate, and the total acquisition time of the measurement [31]. Finally, FNDs with the shallowest depth distributions will offer the lowest LOD, as the magnetic interaction between an N-V defect and a target molecule scales as $1/r^6$.

To assess the utility of dispersed FNDs for sensing, we first identified the most optimal FND size from a range of those currently available. To do this, we evaluated the LOD, sensitivity and dynamic range of the particles by comparing the values of Γ_{int} , C , and p for 50-, 100-, and 140-nm FNDs, sourced from Adamas Nanotechnologies.

Particles were suspended in ultrapure water and sonicated for 30 s to ensure optimal dispersion. The intrinsic T_1 relaxation curve of each FND sample was measured using a 170- μL volume. To provide a similar level of photon shot noise between measurements, data were acquired until approximately 1.2 million photons were collected in the reference window of the first data point. The brightness of each FND sample varied. For example, the 50-nm sample produced less than 1 million counts per second, whereas, the 100- and 140-nm samples were an order of magnitude brighter. Therefore, to ensure the SPAD operated within its linear range, a neutral density filter with an optical density of 1.6 was added to these two samples to reduce the count rate to below 2 million counts per second. Each measurement was replicated three times with a new solution of FNDs.

Figures 3(a)–3(c) show the intrinsic spin relaxation rates Γ_{int} , the spin contrast C , and stretched exponential power p for all replicates and FND sizes. The error bars are derived from the fit error as well as the variation between replicates. Of the three sizes measured, the 100-nm FND sample had the most favorable properties. Specifically, it had the lowest Γ_{int} and smallest relative error, which should translate to the widest dynamic range and highest sensitivity. Additionally, the 100-nm sample provided the largest spin contrast and similar fluorescence intensity compared to the 140-nm FNDs, which enabled relatively high-throughput measurements. The only aspect that was

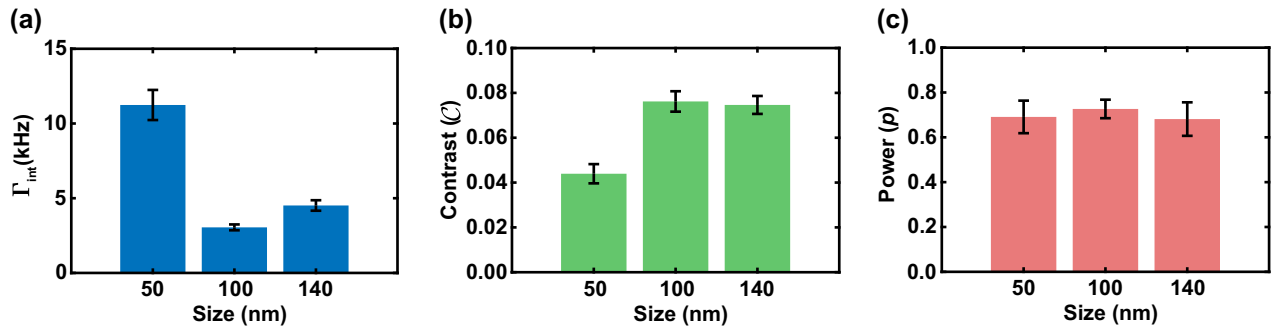


FIG. 3. A comparison of three FND sizes based on the properties of their intrinsic T_1 relaxation curves. (a) spin relaxation rates Γ_{int} , (b) spin contrast C , and (c) stretched exponential powers p for each size.

difficult to assess was the LOD, which is determined by the depth distribution of the N- V defects within the FND ensemble. In principle, the 50 nm particles should offer the lowest LOD, given that they should have a higher proportion of their N- V defects located close to the nanodiamond surface. However, this benefit is outweighed by their high intrinsic relaxation rate and reduced spin contrast. Therefore, we chose to perform sensing measurements using the 100-nm FNDs.

Sensing efficacy was assessed with gadobutrol monohydrate (Sigma Aldrich). The Gd^{3+} ion bound to this ligand has an electron spin of $S = 7/2$, providing a fluctuating magnetic signal that induces a strong response, as shown by the example T_1 relaxation curves in Fig. 4(a). The effect of Gd(III) on the 100-nm FNDs was recorded by first conducting a control measurement of the intrinsic properties of the sample, followed by a sensing measurement after the addition of 30 μL of Gd(III) at various concentrations. Each set of control and sensing measurements was repeated four times.

Figure 4(b) shows Γ_{int} and Γ_{targ} for Gd(III) between 0.1 and 100 mM. The value of Γ_{int} is similar for each control measurement, showing that the spin relaxation properties of the FND ensemble control solutions are consistent. Acquisition of Γ_{int} before each sensing measurement is important as it provides a means of identifying and accounting for changes in the buffer solution or FND spin properties.

The value of Γ_{targ} , on the other hand, increases with increasing Gd(III) concentration, as expected. The shape of the data corresponds well with prior measurements using Gd(III) [32] and Mn(II) [33]. These data also show that the 100-nm FNDs have a dynamic range which spans at least three orders of magnitude. At the minimum concentration probed, 0.1 mM, the signal was $\Gamma_{\text{targ}} = 2 \pm 0.5$ kHz, which suggests the LOD has not yet been reached.

A. Comparison to Conventional Approaches

As a complimentary FND measurement method, this technique circumvents some of the limitations of the

conventional approaches which use confocal or widefield microscopy. To highlight the particular niche that this technique could fill, it is important to discuss the advantages and disadvantages of all three approaches and the circumstances in which each might be the most useful.

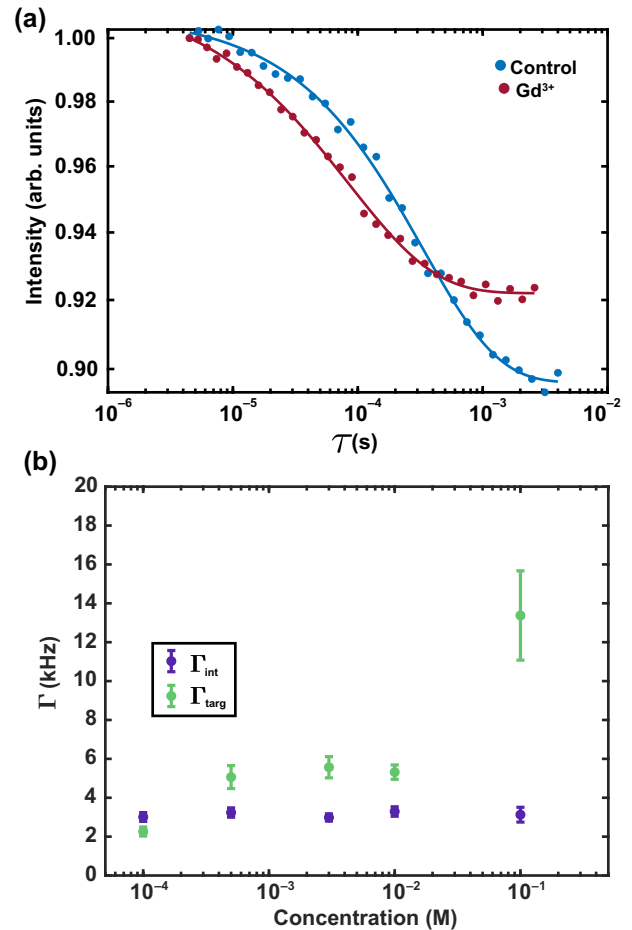


FIG. 4. Sensing Gd(III) using the 100-nm FNDs. (a) Example T_1 relaxation curves from a control measurement and one with Gd(III). There is a large change in Γ between the two curves. (b) Γ_{int} and Γ_{targ} across a range of Gd(III) concentrations between 0.1 and 100 mM.

FNDs are often measured using confocal microscopy, which allows individual particles to be probed. There are numerous examples of confocal microscopy being applied to both characterization of FNDs [15,34–37] and sensing experiments [5,6,8,22,38,39]. The biggest advantage of this approach is that it utilizes the small size of FNDs to provide high spatial resolution, which is of interest in particular applications such as intracellular sensing [8,40–45]. In addition, it is possible to study the effects of specific interventions on individual FNDs, such as chemical termination of the FND surface, by relocating the same particles before and after the modification [16]. The drawbacks of confocal microscopy, however, are that it is extremely time-consuming, requires non-negligible sample preparation, and can be subject to bias. Therefore, confocal microscopy is not an ideal method for certain experiments, especially those that are interested in collecting data over a large spatial area or from many, delocalized, targets.

Widefield microscopy can also be used to measure FNDs, often as a large ensemble [14,19,24,27]. This removes the opportunity for bias that comes with confocal microscopy and provides information about the FND properties at an ensemble level. However, there are several limitations associated with this approach. For example, like confocal microscopy, FNDs must be measured after they are adsorbed onto a 2D substrate due to the relatively narrow focal depth of a microscope objective. In this situation the FNDs must be dried onto the substrate first, to provide a control measurement, followed by the application of the target. The 2D geometry of this approach is suboptimal in certain instances as it does not allow for mixing of the FNDs with a target, especially if the target is also allowed to dry onto the substrate [19]. Finally, it can be challenging to create a thick, uniform layer of FNDs on a 2D substrate [14].

The in-solution technique presented here provides several benefits which complement the confocal and widefield microscopy techniques. For example, the equipment and setup are relatively simple, with only a few optical elements and no microscope objective. The technique also provides high-throughput measurements and reports on FND ensemble behavior. Finally, the 3D, dispersed nature of the FNDs and target ensures that they interact uniformly.

It is also worth comparing this in-solution technique to sensing with a single-crystal diamond. There have been a number of chemical sensing studies utilizing a bulk diamond instead of FNDs [25,32,33,46,47] and it is important to consider the benefits and limitations of this approach as well. In previous work, Steinart *et al.* [32] used a single-crystal diamond fitted with a microfluidic chip to measure Gd(III) across a range of concentrations between 1 and 1000 mM. Comparing the dynamic range and sensitivity of these results to those obtained here, it is interesting that the FNDs performed more favorably in several respects. For example, at a concentration of approximately 100 mM, the

single crystal had a Γ_{targ} of approximately 3 kHz compared to approximately 13 kHz for the FNDs, with a similar relative error between the two. The in-solution technique also provides practical benefits such as being disposable and cheap, compared to single crystal which can be difficult to clean and expensive. Single-crystal measurements also often require an advanced interface such as a microfluidic chip to facilitate liquid sensing experiments.

Single-crystal diamond clearly outperforms the current technique, however, when considering acquisition time; a T_1 relaxation curve can currently be obtained on the time scale of minutes using a single-crystal diamond. This difference is largely due to the acquisition method that we employed in the current setup, which restricts the number of photons that can be detected during each sweep. Modification of the collection apparatus could therefore provide a vast improvement in throughput. To this end, an alternative detector to the SPAD would need to be employed in combination with predetector elements such as an aspheric lens [48], integrating sphere [49], or parabolic lens, which may provide up to 65% collection efficiency [50].

As well as improving the acquisition method, further improvements in throughput could be achieved by understanding the origins of optical noise in the system. Our investigations reveal that the in-solution measurements are approximately a factor of 2 away from the shot noise limit (see the Supplemental Material). The additional optical noise may arise from photon scattering and diffusion of the FNDs themselves, as well as residual laser intensity fluctuations not accounted for by the current common mode rejection scheme. With this level of optical noise we were able to determine changes in the spin relaxation rates with a measurement error of less than 10% when collecting data for about 50 min, which is comparable to the measurement error that can be achieved in a few minutes using a bulk crystal.

In summary, we have demonstrated that T_1 spin relaxometry can be performed on dispersed FNDs in an all-optical cuvette-based system, reporting from approximately 2600 particles simultaneously. We have shown how this system can be used to rapidly assess the suitability of current commercially available FND materials for paramagnetic quantum sensing applications. Using this technique, we found that 100-nm FNDs currently offer the largest dynamic range and highest sensitivity for chemical sensing; however, smaller particles have the potential to reach lower limits of detection. Using 100-nm FNDs, we demonstrated that the in-solution nature of the measurement allows for *in-situ* chemical sensing with a lower limit of detection and wider dynamic range than that shown with a single-crystal diamond, as well as greater throughput than standard confocal or widefield microscopy of FNDs. This measurement platform will also be useful for understanding the effects of surface functionalization on T_1 spin relaxation times [51,52]—providing a method for

assessing the impacts of new terminations with high statistical power and throughput. With straightforward improvements to the collection efficiency, or by implementing a single-point T_1 protocol, this system can be improved further, with the potential to offer subsecond acquisition speeds comparable to a single crystal. Finally, this *in-situ* technique opens the door to alternative sensing paradigms for these nanoscale fluorescent quantum sensors, providing a path to well-controlled, time-resolved measurements of dynamic chemical processes.

The data that support the findings of this study are openly available in Zenodo at <http://doi.org/10.5281/zenodo.7914025>.

ACKNOWLEDGMENTS

The authors would like to acknowledge Dr P. Reineck for supplying the nanodiamond material used in this study. E.G. acknowledges the Graeme Clark Institute for Biomedical Engineering at the University of Melbourne for funding support. The authors would also like to thank the reviewers for their insightful suggestions.

- [1] T. Fujisaku, R. Tanabe, S. Onoda, R. Kubota, T. F. Segawa, F. T. So, T. Ohshima, I. Hamachi, M. Shirakawa, and R. Igarashi, PH nanosensor using electronic spins in diamond, *ACS Nano* **13**, 11726 (2019).
- [2] H. Yukawa, M. Fujiwara, K. Kobayashi, Y. Kumon, K. Miyaji, Y. Nishimura, K. Oshimi, Y. Umehara, Y. Teki, T. Iwasaki, M. Hatano, H. Hashimoto, and Y. Baba, A quantum thermometric sensing and analysis system using fluorescent nanodiamonds for the evaluation of living stem cell functions according to intracellular temperature, *Nanoscale Adv.* **2**, 1859 (2020).
- [3] Y. Nishimura, K. Oshimi, Y. Umehara, Y. Kumon, K. Miyaji, H. Yukawa, Y. Shikano, T. Matsubara, M. Fuki-wara, Y. Baba, and Y. Teki, Wide-field fluorescent nanodiamond spin measurements toward real-time large-area intracellular thermometry, *Sci. Rep.* **11**, 4248 (2021).
- [4] D. A. Simpson, E. Morrisroe, J. M. McCoe, A. H. Lombard, D. C. Mendis, F. Treussart, L. T. Hall, S. Petrou, and L. C. Hollenberg, Non-neurotoxic nanodiamond probes for intraneuronal temperature mapping, *ACS Nano* **11**, 12077 (2017).
- [5] P. C. Tsai, C. P. Epperla, J. S. Huang, O. Y. Chen, C. C. Wu, and H. C. Chang, Measuring nanoscale thermostability of cell membranes with single gold–diamond nanohybrids, *Angew. Chem. – Int. Ed.* **56**, 3025 (2017).
- [6] L. Nie, A. C. Nusantara, V. G. Damle, R. Sharmin, E. P. P. Evans, S. R. Hemelaar, K. J. van der Laan, R. Li, F. P. Perona Martinez, T. Vedelaar, M. Chipaux, and R. Schirhagl, Quantum monitoring of cellular metabolic activities in single mitochondria, *Sci. Adv.* **7**, eabf0573 (2021).
- [7] J. Barton, M. Gulka, J. Tarabek, Y. Mindarava, Z. Wang, J. Schimer, H. Raabova, J. Bednar, M. B. Plenio, F. Jelezko, M. Nesladek, and P. Cigler, Nanoscale dynamic readout of a chemical redox process using radicals coupled with nitrogen-vacancy centers in nanodiamonds, *ACS Nano* **14**, 12938 (2020).
- [8] R. Sharmin, T. Hamoh, A. Sigaeva, A. Mzyk, V. G. Damle, A. Morita, T. Vedelaar, and R. Schirhagl, Fluorescent nanodiamonds for detecting free-radical generation in real time during shear stress in human umbilical vein endothelial cells, *ACS Sens.* **6**, 4349 (2021).
- [9] N. Norouzi, A. C. Nusantara, Y. Ong, T. Hamoh, L. Nie, A. Morita, Y. Zhang, A. Mzyk, and R. Schirhagl, Relaxometry for detecting free radical generation during bacteria's response to antibiotics, *Carbon* **199**, 444 (2022).
- [10] T. Rendler, J. Neburkova, O. Zemek, J. Kotek, A. Zappe, Z. Chu, P. Cigler, and J. Wrachtrup, Optical imaging of localized chemical events using programmable diamond quantum nanosensors, *Nat. Commun.* **8**, 14701 (2017).
- [11] L. P. McGuinness, L. T. Hall, A. Stacey, D. A. Simpson, C. D. Hill, J. H. Cole, K. Ganesan, B. C. Gibson, S. Prawer, P. Mulvaney, F. Jelezko, J. Wrachtrup, R. E. Scholten, and L. C. Hollenberg, Ambient nanoscale sensing with single spins using quantum decoherence, *New J. Phys.* **15**, 073042 (2013).
- [12] J. Tettienne, T. Hingant, L. Rondin, A. Cavaill, L. Mayer, G. Dantelle, T. Gacoin, J. Wrachtrup, J. Roch, and V. Jacques, Spin relaxometry of single nitrogen-vacancy defects in diamond nanocrystals for magnetic noise sensing, *Phys. Rev. B* **87**, 235436 (2013).
- [13] A. Ermakova, G. Pramanik, J.-M. Cai, G. Algara-Siller, U. Kaiser, T. Weil, Y.-K. Tzeng, H. C. Chang, L. P. McGuinness, M. B. Plenio, B. Naydenov, and F. Jelezko, Detection of a few metallo-protein molecules using color centers in nanodiamonds, *Nano Lett.* **13**, 3305 (2013).
- [14] A. Akther, E. P. Walsh, P. Reineck, B. C. Gibson, T. Ohshima, H. Abe, G. McColl, N. L. Jenkins, L. T. Hall, D. A. Simpson, A. R. Rezk, and L. Y. Yeo, Acoustomicrofluidic concentration and signal enhancement of fluorescent nanodiamond sensors, *Anal. Chem.* **93**, 16133 (2021).
- [15] P. Reineck, L. F. Trindade, J. Havlik, J. Stursa, A. Hef-fernan, A. Elbourne, A. Orth, M. Capelli, P. Cigler, D. A. Simpson, and B. C. Gibson, Not all fluorescent nanodiamonds are created equal: A comparative study, *Part. Part. Syst. Charact.* **36**, 1900009 (2019).
- [16] R. G. Ryan, A. Stacey, K. M. O'Donnell, T. Ohshima, B. C. Johnson, L. C. Hollenberg, P. Mulvaney, and D. A. Simpson, Impact of surface functionalization on the quantum coherence of nitrogen-vacancy centers in nanodiamonds, *ACS Appl. Mater. Interfaces* **10**, 13143 (2018).
- [17] S. K. Padamati, T. A. Vedelaar, F. P. Martinez, A. C. Nusantara, and R. Schirhagl, Insight into a Fenton-like reaction using nanodiamond based relaxometry, *Nanomaterials* **12**, 2422 (2022).
- [18] R. Li, T. Vedelaar, A. Mzyk, A. Morita, S. K. Padamati, and R. Schirhagl, Following polymer degradation with nanodiamond magnetometry, *ACS Sens.* **7**, 123 (2022).
- [19] F. Gorrini, R. Giri, C. E. Avalos, S. Tambalo, S. Mannucci, L. Basso, N. Bazzanella, C. Dorigoni, M. Cazzanelli, P. Marzola, A. Miotello, and A. Bifone, Fast and sensitive detection of paramagnetic species using coupled charge and spin dynamics in strongly fluorescent nanodiamonds, *ACS Appl. Mater. Interfaces* **11**, 24412 (2019).

- [20] D. A. Hopper, H. J. Shulevitz, and L. C. Bassett, Spin readout techniques of the nitrogen-vacancy center in diamond, *Micromachines* **9**, 437 (2018).
- [21] H. Jayakumar, S. Dhomkar, J. Henshaw, and C. A. Meriles, Spin readout via spin-to-charge conversion in bulk diamond nitrogen-vacancy ensembles, *Appl. Phys. Lett.* **113**, 122404 (2018).
- [22] A. Laraoui, J. S. Hodges, and C. A. Meriles, Nitrogen-vacancy-assisted magnetometry of paramagnetic centers in an individual diamond nanocrystal, *Nano. Lett.* **12**, 3477 (2012).
- [23] J. M. McCoe, M. Matsuoka, R. W. de Gille, L. T. Hall, J. A. Shaw, J. P. Tetienne, D. Kisailus, L. C. Hollenberg, and D. A. Simpson, Quantum magnetic imaging of iron biomineralization in teeth of the chiton *Acanthopleura hirtosa*, *Small Methods* **4**, 1900754 (2020).
- [24] M. Sow, H. Steuer, S. Adekanye, L. Ginés, S. Mandal, B. Gilboa, O. A. Williams, J. M. Smith, and A. N. Kapanidis, High-throughput nitrogen-vacancy center imaging for nanodiamond photophysical characterization and pH nanosensing, *Nanoscale* **12**, 21821 (2020).
- [25] D. A. Simpson, R. G. Ryan, L. T. Hall, E. Panchenko, S. C. Drew, S. Petrou, P. S. Donnelly, P. Mulvaney, and L. C. Hollenberg, Electron paramagnetic resonance microscopy using spins in diamond under ambient conditions, *Nat. Commun.* **8**, 458 (2017).
- [26] T. A. Vedelaar, T. H. Hamoh, F. p. Perona Martínez, M. Chipaux, and R. Schirhagl, Optimising data processing for nanodiamond based relaxometry, *Adv. Quantum Technol.* **2300109**, 1 (2023).
- [27] S. Eldemrashed, G. Thalassinou, A. Alzahrani, Q. Sun, E. Walsh, E. Grant, H. Abe, T. L. Greaves, T. Ohshima, P. Cigler, P. Matejcek, D. Simpson, A. D. Greentree, G. Bryant, B. C. Gibson, and P. Reineck, Fluorescent HPHT nanodiamonds have disk- and rod-like shapes, *Carbon* **206**, 268 (2023).
- [28] See the Supplemental Material at <http://link.aps.org/supplemental/10.1103/PhysRevApplied.20.034018> for further information on how the all-optical protocol was optimized. The Supp Info also contains references [12,26–28,32,42,53,54].
- [29] L. B. Casabianca, A. I. Shames, A. M. Panich, O. Shenderova, and L. Frydman, Factors affecting DNP NMR in polycrystalline diamond samples, *J. Phys. Chem. C* **115**, 19041 (2011).
- [30] J. Austin, C. Minelli, D. Hamilton, M. Wywijas, and H. J. Jones, Nanoparticle number concentration measurements by multi-angle dynamic light scattering, *J. Nanopart. Res.* **22**, 108 (2020).
- [31] J. D. A. Wood, D. A. Broadway, L. T. Hall, A. Stacey, D. A. Simpson, J.-P. Tetienne, and L. C. L. Hollenberg, Wideband nanoscale magnetic resonance spectroscopy using quantum relaxation of a single spin in diamond, *Phys. Rev. B* **94**, 155402 (2016).
- [32] S. Steinert, F. Ziem, L. T. Hall, A. Zappe, M. Schweikert, N. Gotz, A. Aird, G. Balasubramanian, L. Hollenberg, and J. Wrachtrup, Magnetic spin imaging under ambient conditions with sub-cellular resolution, *Nat. Commun.* **4**, 1607 (2013).
- [33] F. C. Ziem, N. S. Götz, A. Zappe, S. Steinert, and J. Wrachtrup, Highly sensitive detection of physiological spins in a microfluidic device, *Nano Lett.* **13**, 4093 (2013).
- [34] J. P. Boudou, J. Tisler, R. Reuter, A. Thorel, P. A. Curmi, F. Jelezko, and J. Wrachtrup, Fluorescent nanodiamonds derived from HPHT with a size of less than 10 nm, *Diam. Relat. Mater.* **37**, 80 (2013).
- [35] H. Yamano, S. Kawai, K. Kato, T. Kageura, M. Inaba, T. Okada, I. Higashimata, M. Haruyama, T. Tani, K. Yamada, S. Onoda, W. Kada, O. Hanaizumi, T. Teraji, J. Isoya, and H. Kawarada, Charge state stabilization of shallow nitrogen vacancy centers in diamond by oxygen surface modification, *Jpn. J. Appl. Phys.* **56**, 04CK08 (2017).
- [36] C. Laube, T. Oeckinghaus, J. Lehnert, J. Griebel, W. Knolle, A. Denisenko, A. Kahnt, J. Meijer, J. Wrachtrup, and B. Abel, Controlling the fluorescence properties of nitrogen vacancy centers in nanodiamonds, *Nanoscale* **11**, 1770 (2019).
- [37] B. D. Wood, G. A. Stimpson, J. E. March, Y. N. D. Lekhai, C. J. Stephen, B. L. Green, A. C. Frangeskou, L. Ginés, S. Mandal, O. A. Williams, and G. W. Morley, Long spin coherence times of nitrogen vacancy centres in milled nanodiamonds, *Phys. Rev. B* **105**, 205401 (2022).
- [38] M. Fujiwara, R. Tsukahara, Y. Sera, H. Yukawa, Y. Baba, S. Shikata, and H. Hashimoto, Monitoring spin coherence of single nitrogen-vacancy centers in nanodiamonds during pH changes in aqueous buffer solutions, *RSC Adv.* **9**, 12606 (2019).
- [39] F. Perona Martínez, A. C. Nusantara, M. Chipaux, S. K. Padamati, and R. Schirhagl, Nanodiamond relaxometry-based detection of free-radical species when produced in chemical reactions in biologically relevant conditions, *ACS Sens.* **5**, 3862 (2020).
- [40] C. Y. Fang, V. Vijayanthimala, C. A. Cheng, S. H. Yeh, C. F. Chang, C. L. Li, and H. C. Chang, The exocytosis of fluorescent nanodiamond and its use as a long-term cell tracker, *Small* **7**, 3363 (2011).
- [41] C.-C. Fu, H.-Y. Lee, K. Chen, T.-S. Lim, H.-Y. Wu, K. Lin, P.-K. Wei, C.-C. Fu, H.-Y. Lee, K. Chen, T.-S. Lim, H.-Y. Wu, P.-K. Lin, P.-K. Wei, P.-H. Tsao, H.-C. Chang, and W. Fann, Characterization and application of single fluorescent nanodiamonds as cellular biomarkers, *Proc. Natl. Acad. Sci.* **104**, 727 (2007).
- [42] L. P. McGuinness, Y. Yan, A. Stacey, D. A. Simpson, L. T. Hall, D. Maclaurin, S. Praver, P. Mulvaney, J. Wrachtrup, F. Caruso, R. E. Scholten, and L. C. Hollenberg, Quantum measurement and orientation tracking of fluorescent nanodiamonds inside living cells, *Nat. Nanotechnol.* **6**, 358 (2011).
- [43] A. Kuwahata, M. Sekino, T. Imaoka, S. Kakinuma, T. Sugi, W. Kada, O. Hanaizumi, and R. Igarashi, All-optical wide-field selective imaging of fluorescent nanodiamonds in cells, in vivo and ex vivo, *ACS Nano* **15**, 12869 (2021).
- [44] L. Nie, A. C. Nusantara, V. G. Damle, M. V. Baranov, M. Chipaux, C. Reyes-San-Martin, T. Hamoh, C. P. Epperla, M. Guricova, P. Cigler, G. van den Bogaart, and R. Schirhagl, Quantum sensing of free radicals in primary human dendritic cells, *Nano Lett.* **22**, 1818 (2022).
- [45] A. Morita, A. C. Nusantara, A. Myzk, F. P. Perona Martínez, T. Hamoh, V. G. Damle, K. J. van der Laan, A.

- Sigaeva, T. Vedelaar, M. Chang, M. Chipaux, and R. Schirhagl, Detecting the metabolism of individual yeast mutant strain cells when aged, stressed or treated with antioxidants with diamond magnetometry, *Nano Today* **48**, 101704 (2023).
- [46] V. Radu, J. C. Price, S. J. Levett, K. K. Narayanasamy, T. D. Bateman-Price, P. B. Wilson, and M. L. Mather, Dynamic quantum sensing of paramagnetic species using nitrogen-vacancy centers in diamond, *ACS Sens.* **5**, 703 (2020).
- [47] E. S. Grant, L. T. Hall, L. C. L. Hollenberg, G. Mccoll, and D. A. Simpson, Nonmonotonic superparamagnetic behavior of the ferritin iron core revealed via quantum spin relaxometry, *ACS Nano* **17**, 372 (2023).
- [48] J. L. Webb, L. Troise, W. Hansen, J. Ahcard, O. Brinza, R. Staacke, M. Kieschnick, J. Meijer, J.-F. Perrier, K. Berg-Sorensen, A. Huck, and U. Andersen Lund, Optimization of a diamond nitrogen vacancy centre magnetometer for sensing of biological signals, *Front. Phys.* **8**, 522536 (2020).
- [49] S. V. Koniakhin, M. K. Rabchinskii, N. A. Besedina, L. V. Sharonova, A. V. Shvidchenko, and E. D. Eidelman, Evidence of absorption dominating over scattering in light attenuation by nanodiamonds, *Phys. Rev. Res.* **2**, 013316 (2020).
- [50] T. Wolf, P. Neumann, K. Nakamura, H. Sumiya, T. Ohshima, J. Isoya, and J. Wrachtrup, Subpicotesla Diamond Magnetometry, *Phys. Rev. X* **5**, 041001 (2015).
- [51] A. Wolcott, T. Schiros, M. E. Trusheim, E. H. Chen, D. Nordlund, R. E. Diaz, O. Gaathon, D. Englund, and J. S. Owen, Surface structure of aerobically oxidized diamond nanocrystals, *J. Phys. Chem. C* **118**, 26695 (2014).
- [52] A. Stacey, N. Dontschuk, J. P. Chou, D. A. Broadway, A. K. Schenk, M. J. Sear, J. P. Tetienne, A. Hoffman, S. Praver, C. I. Pakes, A. Tadich, N. P. de Leon, A. Gali, and L. C. Hollenberg, Evidence for primal sp^2 defects at the diamond surface: Candidates for electron trapping and noise sources, *Adv. Mater. Interfaces* **6**, 1801449 (2019).
- [53] J. Choi, S. Choi, G. Kucsko, P. C. Maurer, B. J. Shields, H. Sumiya, S. Onoda, J. Isoya, E. Demler, F. Jelezko, N. Y. Yao, and M. D. Lukin, Depolarization Dynamics in a Strongly Interacting Solid-State Spin Ensemble, *Phys. Rev. Lett.* **118**, 093601 (2017).
- [54] R. Giri, C. Dorigoni, S. Tambalo, F. Gorrini, and A. Bifone, Selective measurement of charge dynamics in an ensemble of nitrogen-vacancy centers in nanodiamond and bulk diamond, *Phys. Rev. B* **99**, 155426 (2019).